Mouse genomic associations with *in vitro* sensitivity to simulated space radiation

Egle Cekanaviciute [a], Duc Tran [b], Hung Nguyen [b], Alejandra Lopez Macha [a,c], Eloise Pariset [a,d], Sasha Langley [e], Giulia Babbi [f], Sherina Malkani [a,c], Sébastien Penninckx [e,g], Jonathan C. Schisler [h], Tin Nguyen [b], Gary H. Karpen [e], Sylvain.V. Costes [a,*]

[a] *Space Biosciences Division, NASA Ames Research Center, Moffett Field, CA 94035, USA*
[b] *Department of Computer Science and Engineering, University of Nevada, Reno, NV 89557, USA*
[c] *Blue Marble Space Institute of Science, 600 1st Avenue, 1st Floor, Seattle, WA 98104, USA*
[d] *Universities Space Research Association, 615 National Avenue, Mountain View, CA 94043, USA*
[e] *Molecular and Cell Biology, UC Berkeley, Berkeley, CA 94720, USA, and Biological Systems and Engineering Division, Lawrence Berkeley National Laboratory, 1 Cyclotron Rd, Berkeley, CA 94720, USA*
[f] *Bologna Biocomputing Group, FABIT, University of Bologna, Via Belmeloro 6, Bologna, Italy*
[g] *Medical Physics Department, Jules Bordet Institute, Université Libre de Bruxelles, 90 Rue Meylemeersch, 1070 Brussels, Belgium*
[h] *McAllister Heart Institute and Department of Pharmacology, The University of North Carolina at Chapel Hill, NC 27599, USA*

ARTICLE INFO

ABSTRACT

Exposure to ionizing radiation is considered by NASA to be a major health hazard for deep space exploration missions. Ionizing radiation sensitivity is modulated by both genomic and environmental factors. Understanding their contributions is crucial for designing experiments in model organisms, evaluating the risk of deep space (*i.e.* high-linear energy transfer, or LET, particle) radiation exposure in astronauts, and also selecting therapeutic irradiation regimes for cancer patients. We identified single nucleotide polymorphisms in 15 strains of mice, including 10 collaborative cross model strains and 5 founder strains, associated with spontaneous and ionizing radiation-induced *in vitro* DNA damage quantified based on immunofluorescent tumor protein p53 binding protein (53BP1) positive nuclear foci. Statistical analysis suggested an association with pathways primarily related to cellular signaling, metabolism, tumorigenesis and nervous system damage. We observed different genomic associations in early (4 and 8 h) responses to different LET radiation, while later (24 hour) DNA damage responses showed a stronger overlap across all LETs. Furthermore, a subset of pathways was associated with spontaneous DNA damage, suggesting 53BP1 positive foci as a potential biomarker for DNA integrity in mouse models. Our results suggest several mouse strains as new models to further study the impact of ionizing radiation and validate the identified genetic loci. We also highlight the importance of future human *in vitro* studies to refine the association of genes and pathways with the DNA damage response to ionizing radiation and identify targets for space travel countermeasures.

1. Introduction

Interest in human deep space exploration has increased significantly over the last decade, especially focusing on detrimental health effects caused by ionizing radiation beyond the protective magnetic field of the Earth (Durante and Cucinotta, 2008). For example, a Mars mission estimated to last nearly three years will expose astronauts to radiation doses of up to 1 Sv, which is considered to increase cancer risk significantly (Cucinotta and Durante, 2006). The most biologically concerning source of ionizing radiation beyond the Earth's magnetosphere is galactic cosmic rays (GCRs), composed of 90% energetic protons, 9% ^{4}He nuclei and 1% high mass-high charge (HZE) particles. HZE particles are ions between ^{4}He and ^{56}Fe that induce significant biological damage due to their high linear energy transfer (LET), and are only partially mitigated by protective shielding (Cucinotta and Durante, 2006; Durante and Cucinotta, 2008). Therefore, understanding the biological effects of HZE particles is essential for identifying biomarkers for individual sensitivity and resistance and developing countermeasures to

reduce astronaut health risks.

One of the main adverse effects of exposure to ionizing radiation, especially HZE particles, is DNA damage (Cardis et al., 1995, 2007; National Research, 2006), which leads to carcinogenesis, central nervous system impairments(Azizova et al., 2020; Pasqual et al., 2021), immune dysregulation (Braganza et al., 2012; Gasser et al., 2005) and circulatory system effects (Tapio et al., 2021; Wang et al., 2016). An early mouse experiment has shown that HZE particles have a relative biological effectiveness (RBE) as high as 40 for 600 MeV/n ^{56}Fe particles causing Harderian gland tumors (Alpen et al., 1993, 1994). Because these studies only used one mouse strain, the scientific community has not been able to infer whether the effect was associated with strain-dependent radiosensitivity. In addition, such gland does not exist in humans, making it difficult to assess the relevance of the findings for cancer risks for astronauts.

Although the carcinogenic and DNA damage-related effects of HZE particles in animal models and human cells are the focus of numerous studies, the genomic and environmental factors that contribute to *individual* sensitivity among subjects remain elusive (Barcellos-Hoff et al., 2015; Cucinotta et al., 2017). In addition, radiogenic tumors have been shown to depend on the strain of mice (Kaplan et al., 1956), as well as the histotype of the tumor (Edmondson et al., 2020) and tissue specificity and exclusivity. Thus, understanding the genes and pathways linked with HZE particle sensitivity may suggest mechanisms to be targeted for developing countermeasures to avoid the radiation hazards during prolonged space travel.

In order to identify mouse genes associated with space radiation risks, we used the *collaborative cross* (CC) mice (Churchill et al., 2004), a panel of recombinant inbred strains that captures 90% of the known variation among laboratory mice. This system allows high-resolution mapping of genomic associations with different phenotypes, including diseases and reactions to various environmental stressors, due to their genomic diversity and long-term genetic stability. The U.S. Department of Energy Low Dose Scientific Focus Area utilized CC mouse model due to the high levels of genetic variation distributed randomly across the strain genomes (Snijders et al., 2016). This model enhances the probability of genomic associations to phenotypes using a relatively small number of strains and permits other investigators to study the phenotypes of interest further by replicating the same specific, individual genotypes of mouse strains.

In this work, we utilized the CC model to identify genetic associations with *in vitro* DNA damage responses. We and others have previously reported that biomarkers labeling DNA double strand breaks are suitable surrogate markers of sensitivity to ionizing radiation (Ochola et al., 2019; Pariset et al., 2020b; Penninckx et al., 2019, 2020; Rube et al., 2008). More recently, our group used *in vitro* samples from a combination of 15 mouse strains (5 inbred and 10 CC) to demonstrate that both their baseline levels of spontaneous DNA damage and their dose responses to ionizing radiation were highly variable among different strains based on quantification of immunofluorescent foci of tumor suppressor p53-binding protein 1 (53BP1) (Pariset et al., 2020b; Penninckx et al., 2019), which is a key component of DNA double-stranded break repair. Here we followed up on this result by conducting an exploratory low-coverage genome-wide association study (GWAS) using the same 15 mouse strains to identify single nucleotide polymorphisms (SNPs) and pathways associated with spontaneous DNA damage, as well as DNA damage responses to different types of ionizing radiation. Specifically, we compared the responses to low-LET X-rays and two types of HZE particle irradiation (350 MeV/n ^{40}Ar at 104 keV/μm LET; and 600 MeV/n ^{56}Fe at 170 keV/μm LET) at different doses and post-irradiation time points. We further evaluated the pathways associated with responses to HZE particles due to their relevance to health risks during deep space exploration.

By identifying candidate genes and pathways related to space health risks, we provide new directions for selecting the appropriate mouse models for space biology and space radiation studies: different mouse strains might be more suitable for analyzing high- *vs*. low-LET responses and different aspects of DNA damage and repair kinetics. Our results also suggest targets for evaluating and mitigating DNA damage caused by deep space radiation at the level of an individual subject, opening the door for precision space medicine. All raw data and associated genotypes for each animal are available in the Open Science NASA platform GeneLab, a life science database focused on spaceflight- relevant experiments with the highest standards for rich metadata (Berrios et al., 2021) and curated radiation dosimetry information (Beheshti et al., 2018), which are essential features to enable further mining of these data by the scientific community.

2. Materials and methods

2.1. Mouse strains

Collaborative Cross (CC) mice are inbred mice designed by the Jackson Laboratory (Bar Harbor, ME) and developed at University of North Carolina, Chapel Hill (Srivastava et al., 2017) that are derived from five classic inbred strains (A/J, C57BL/6, 129S1/SvImJ, NOD/-ShiltJ and NZO/H1LtJ) and three wild-derived sub-strains (CAST/EiJ, PWK/PhJ and WSB/EiJ). 10 mouse strains from the CC panel - CC002, CC011, CC013, CC019, CC032, CC037, CC040, CC042, CC051 and CC061 - were chosen for our experiment. In addition to CC mice strains, five inbred reference strains: C57BL/6 J, BALB/cByJ, B6C3F, C3H/HeMsNsrf and CBA/CaJ were also included in this study. In total, 72 animals were used, with 37 females and 35 males.

2.2. Irradiation

Detailed experimental methods for cell extraction and irradiation are described in our previous work (Penninckx et al., 2019). All experiments were performed following IACUC protocol no. 306,002; Lawrence Berkeley National Laboratory (LBNL), Berkeley, CA according to National Research Council guide for care and use of laboratory animals. X-ray experiments were conducted at LBNL using a 160-kVp Faxitron X-ray machine (Lincolnshire, IL), while particle irradiation experiments were conducted at NASA Space Radiation Laboratory (NSRL) beam line at Brookhaven National Laboratory (Upton, NY).

Briefly, skin fibroblasts from ear punches were collected from mice at 10–12 weeks of age, grown as primary cell cultures and frozen at different passages. Cells were thawed and grown for 24 – 48 h before being irradiated with X-rays or two different HZE particles: 350 MeV/n ^{40}Ar and 600 MeV/n ^{56}Fe, which have 104 and 170 keV/μm LET, respectively. At the time of irradiation, fibroblasts were 80% confluent for ^{40}Ar and 90% confluent for ^{56}Fe. For particle irradiations, two fluences (1.1 and 3 particles/100 μm^2) were used, corresponding to four distinct doses depending on their respective LET (0.30 and 0.82 Gy for 600 MeV/n ^{56}Fe; 0.18 and 0.50 Gy for 350 MeV/n ^{40}Ar). For X-ray irradiation, 0.1 and 1 Gy doses were used instead. The dose rate for both X-ray and particle irradiations was 1 Gy/min.

2.3. Immunocytochemistry

At 4, 24 and 48 h post-irradiation, with an additional time point at 8 h for 600 MeV/n ^{56}Fe particle irradiations, cells were fixed with 4% paraformaldehyde (Electron Microscopy Sciences, Hatfield, PA) in phosphate buffered saline (PBS) for 15 min at room temperature. After the incubation period, cells were washed with PBS 3 times, 5 min each for the total of 15 min. Plates were then filled with PBS (300 μl/well), sealed and kept at 4°C until immunostaining. All experiments were performed in duplicate.

For immunostaining 53BP1 to quantify DNA double strand breaks, cells were washed with PBS, permeabilized with 0.1% Triton-X for 20 min and blocked with 3% BSA in PBS for 1 hour. Cells were then incubated in a rabbit polyclonal anti-53BP1 primary antibody (Bethyl Labs

#IHC-00,001) at 1:400 in blocking buffer (3% BSA in PBS) for 1 hour, followed by 2 washes in 0.1% Tween-20 in PBS and a subsequent incubation with Alexa Fluor 488 goat anti-rabbit secondary antibody (ThermoFisher Scientific #A11034) at 1:400 in blocking buffer for 1 hour, followed by 2 washes in 0.1% Tween-20 in PBS. Nuclear staining was performed with DAPI at 1:1000 in PBS for 5 min (ThermoFisher Scientific, #D1306), followed by 2 final washes in 0.1% Tween-20 in PBS and resuspension in PBS.

2.4. Imaging

After staining, cells were imaged and quantified using a high-throughput semi-automated microscope developed in-house by our group (40 × 0.95 NA dry lens, Nikon), and images were analyzed using an automated nuclear foci quantification MATLAB® algorithm previously published by our group (Pariset et al., 2020a; Penninckx et al., 2019). The foci quantification was set at a target of at least 800 cells per sample based on previous publications (Costes et al., 2007). All raw data are available online (see Data Availability), while images and quantification algorithm are available upon request.

2.5. Genotyping

Genomic DNA was extracted from fibroblasts obtained from each individual mouse from each of the five non-CC inbred strains using AllPrep DNA/RNA Mini kit (Qiagen, #80,204). The concentration and purity of extracted DNA was determined using a NanoDrop 2000 UV–vis spectrophotometer (ThermoFisher Scientific) based on 260 nm/280 nm and 260 nm/230 nm ratios. All DNA samples contained a minimal concentration of 20 ng/μL and were shipped to GeneSeek (Neogen Genomics, Lincoln, NE, USA). SNP analysis was conducted using Mega-Mouse Universal Genotyping Array (MegaMUGA platform). The original MUGA array was developed on Illumina Infinium platform in cooperation with Neogen Inc and contained 7851 SNP markers all spaced uniformly approximately ~325 kb across the mouse reference genome. The MegaMUGA SNP array that was used provided a 10-fold higher marker density than MUGA (77,808 markers) and additional 14,000 probes detecting variants segregating in wild-derived strains. Collaborative cross genotypes were obtained from the GigaMUGA database (Morgan et al., 2015). Only the overlapping SNPs that were found in both platforms were used for all analysis.

2.6. Radiosensitivity and DNA repair phenotypes

As published previously (Pariset et al., 2020b; Penninckx et al., 2019), spontaneous DNA damage (Background; BGD) phenotype for each mouse strain was defined as the average number of 53BP1$^+$ foci per nucleus in the control group (0 Gy sham irradiation), assessed at 4 different time points: 4, 8, 24 and 48 h for all three radiation qualities, averaged across all analyses after removing statistical outlier values (2 standard deviations above or below the mean for each strain).

Radiation-induced DNA damage (Foci per Gray; FPG) phenotype was defined as the average increase in 53BP1$^+$ foci per nucleus, per 1 Gy of irradiation. The FPG phenotype was quantified in response to irradiation by X-rays and HZE particles (350 MeV/n ^{40}Ar, 600 MeV/n ^{56}Fe), averaged per mouse strain, separately for each radiation quality and time point.

2.7. Genotype-phenotype associations

The significance of SNP-phenotype associations was determined using the R *qtl2* package (Broman et al., 2019) that includes kinship information between samples. For FPG calculation in response to each radiation quality, time points were used as covariates. The following linear model was used to infer the relationship between phenotype and genotype:

num_foci_irradiated_i ~ genotype_i + kinship_adjustment_i + time_point_i + error_i,

where *i* indexes the mouse.

The output of this calculation is the LOD (limit of detection) score for each SNP. LOD scores can be converted to p-value using:

$$P(LOD)=0.5*(\chi^2>2*\log_{10}(LOD))$$

where $2*\log_{10}(LOD)$ follows the chi-square distribution with degree of freedom = 1 (Nyholt, 2000).

2.8. SNP annotation and pathway analysis

Supplementary Figure 1 shows the overall workflow of pathway analysis. The *p* values for each SNP were calculated using *qtl2* R package and serve as an input of the workflow. Bioconductor package *BiomaRt v.105* (Durinck et al., 2005, 2009) was used to get gene annotations and positions, mapping SNPs within 25,000 bp of a gene. *Reactome v.78* (Jassal et al., 2020) was used to get pathway information.

For each gene, the p-values of the SNPs were merged using two different methods: Fisher and the additive method addCLT (Nguyen et al., 2016). The Fisher method produces a list of *p* values, one value per gene. These *p* values are subsequently used either to create a pre-ranked gene list using fast gene set enrichment analysis FGSEA (Korotkevich et al., 2021) or correct them using False Discovery Rate (FDR) with a threshold of 0.05 to select differentially expressed genes for hypergeometric test using over representation analysis (ORA), and both FGSEA and ORA are used for pathway analysis. Thus, our analysis results in 4 lists of pathway *p* values, generated by the following combinations of methods: Fisher/FGSEA, Fisher/ORA, addCLT/FGSEA, addCLT/ORA.

For each pathway, these 4 *p* values are combined using addCLT to produce a single additive *p* value per pathway. The additive p-values of all pathways are then corrected using FDR. The final pathways with FDR-corrected p-values <0.05 are considered significantly associated with the phenotype (either BGD, or FPG for each radiation type and time point). Our main motivations behind combining *p* values at the end of the pipeline are a) accounting for multiple sources of weak but consistent evidence and b) combining the evidence generated by different methods to prevent the flaws of any individual method from compromising the results. All pathway graphs were created using R packages *ggplot2, ggraph, igraph* and *UpSetR*.

All code used for the analysis will be available in Supplementary Materials (see **Data and Code Availability** section) upon publication.

3. Results

3.1. Experimental approach

Our study aimed to identify the genetic differences and biological mechanisms responsible for the variability of DNA damage responses to ionizing radiation established in previous investigations of 15 mouse strains (5 inbred, 10 CC) that had been established in previous investigations (Penninckx et al., 2019). DNA damage response patterns were defined by quantifying 53BP1$^+$ radiation-induced foci between 4 h and 48 h post-irradiation in mouse skin fibroblasts irradiated *in vitro*. We used two doses of low-LET X-rays (0.1 and 1 Gy), and two fluences of high-LET 350 MeV/n ^{40}Ar and 600 MeV/n ^{56}Fe ions (1.1 and 3 particles/100μm^2, which respectively correspond to 0.18 and 0.5 Gy for 350 MeV/n ^{40}Ar, and 0.3 and 0.82 Gy for 600 MeV/n ^{56}Fe). The experimental design is depicted in Fig. 1A.

Our experimental design allowed us to evaluate two aspects of DNA damage responses to ionizing radiation: the severity of initial damage and the speed and effectiveness of subsequent repair. The time course of DNA double strand break repair depends on the pathway involved: non-homologous end joining takes up to 2 h after irradiation, while homologous recombination requires at least 8 h (Ingram et al., 2019; Kim et al.,
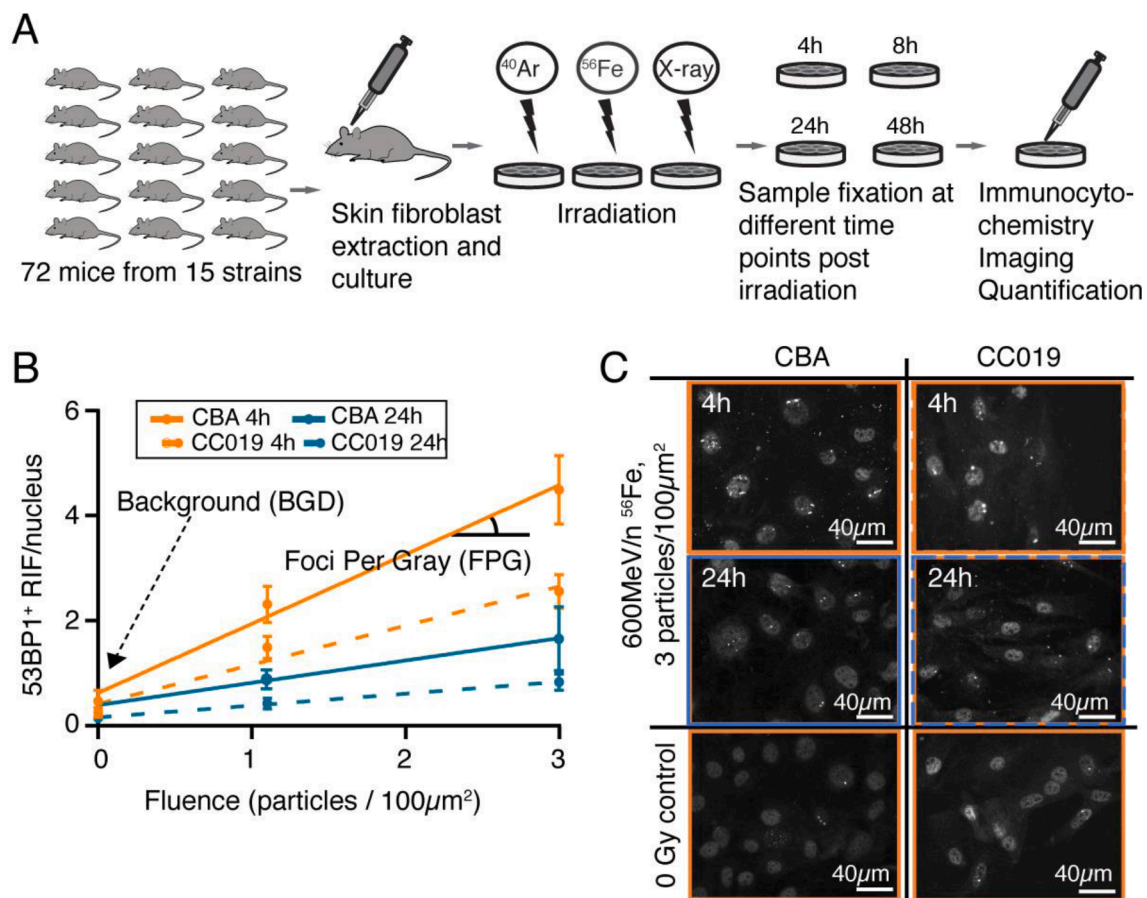
Fig. 1. Quantification of radiation-induced DNA damage in 15 mouse strains. A. Experimental design. **B.** Representative graph showing Foci Per Gray (FPG) and Background (BGD) phenotypes in two mouse strains (CBA and CC019) at two time points (4 h and 24 h) post-irradiation as a function of 600 MeV/n ^{56}Fe radiation fluence (data points at 1.1 and 3 particles/100μm²). **C.** Representative images showing 53BP1$^+$ DNA double stranded break repair foci in the same mouse strains at 4 h and 24 h post-irradiation with 600 MeV/n ^{56}Fe particles at the fluence of 3 particles/100μm² and in sham-irradiated control.

2005; Penninckx et al., 2021). Thus, 4 and 8 hour timepoints include both repair processes that involve 53BP1 accumulation at DNA damage sites (Shibata and Jeggo, 2020). Although double strand breaks are formed earlier than 4 after irradiation, earlier quantification was not feasible given experimental limitations. DNA double strand breaks are repaired over the next 24 – 48 h, and the damage that remains afterwards is considered persistent. Notably, unrepaired DNA damage *in vitro* at 24 h post irradiation has previously been associated with *in vivo* carcinogenesis in mouse models, making 24 h a relevant timepoint to examine as a potential biomarker of mouse strain radioresistance (Ochola et al., 2019; Pariset et al., 2020b).

We used two radiation response-relevant phenotypes for GWAS (Fig. 1B.) The first is Foci Per Gray (FPG), a quantification of the irradiation response using the average number of 53BP1$^+$ DNA repair foci per nucleus, per radiation dose (in Gy), measured at each time point for each radiation quality and mouse strain. FPG numbers followed previously reported kinetics of increasing at early time points (4 h and 8 h) post-irradiation that reflects ionizing radiation-induced DNA damage, followed by a gradual decrease at later time points (24 h and 48 h) due to ongoing DNA repair (Pariset et al., 2020b). FPG differences between strains for early time points also reflect the amount of double-strand break DSB clustering into DNA repair domains, a phenotype critical for high-LET radiation risk (Neumaier et al.; Vadhavkar et al., 2014), since increased clustering is associated with lower repair and worse physiological outcomes. Representative images from *in vitro* irradiated fibroblasts from two mouse strains with low and high FPG, CC019 and CBA, respectively, are shown in Fig. 1C at 4 h and 24 h after 600 MeV/n ^{56}Fe irradiation and in sham conditions.

The second measured phenotype is Background (BGD), which is the average number of 53BP1$^+$ foci at sham irradiation conditions, and reflects the amount of spontaneous DSBs. BGD was averaged for each strain across all irradiation experiments and all time points, after excluding statistical outliers (>2 standard deviations above or below the mean for the strain). Notably, although both male and female mice were used as a source of *in vitro* cells, we did not observe sexual dimorphism in any FPG or BGD values.

To identify SNPs associated with FPG and BGD phenotypes, we performed a GWAS based on sequencing the five inbred strains and known genotypes from the ten CC strains, accounting for kinship (described in **Materials and Methods**). Fig. 2 shows representative Manhattan plots depicting the *p* values of the associations between SNPs and FPG 4 h post-irradiation with X-rays, 350 MeV/n ^{40}Ar and 600 MeV/n ^{56}Fe, as well as background DNA repair foci. All SNP-phenotype associations are listed in Suppl. Table 1.

3.2. Genes and pathways associated with background DNA repair and responses to ionizing radiation

We characterized the quantitative trait loci (QTLs) linked with the SNPs identified by our GWAS analysis. SNPs were mapped to a gene if they fell within 25,000 base pairs of the gene. The resulting set of genes was analyzed using an additive approach of the Fisher method and addCLT to identify the genes with FDR-adjusted *p* values below 0.05, which were then mapped to pathways using the Reactome database. Significantly enriched pathways were identified using FGSEA and ORA test, and p values from each method were combined using addCLT to
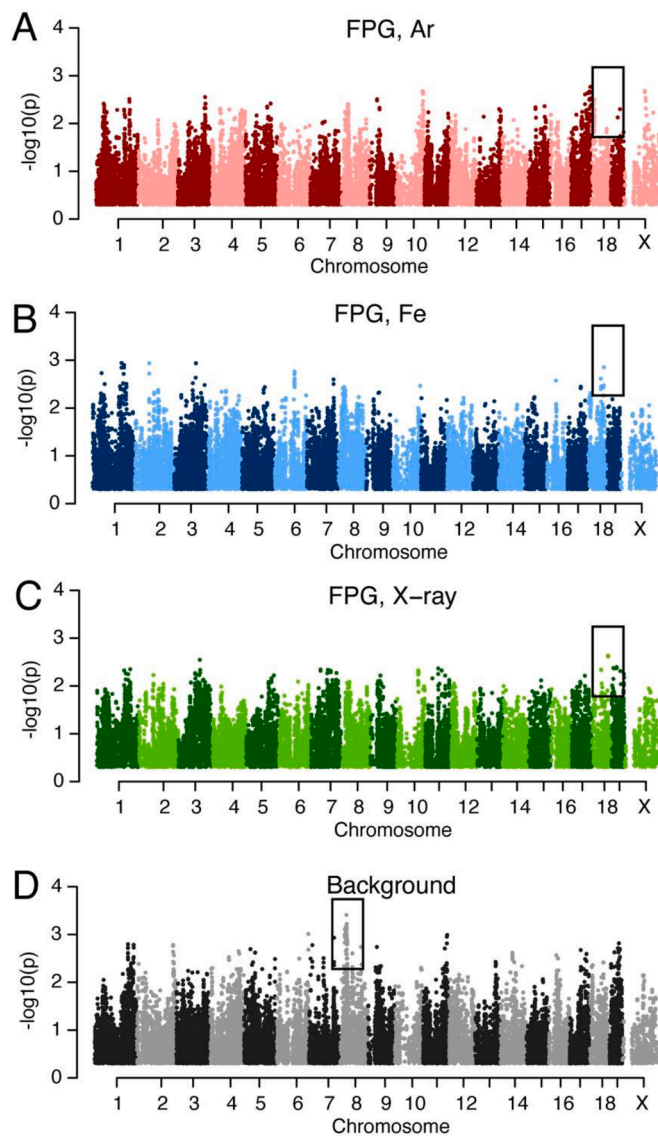
Fig. 2. SNPs associated with DNA repair after irradiation and spontaneous DNA damage. Quantification was performed 4 h post-irradiation by X-rays and high-LET particles (^{40}Ar, ^{56}Fe). X-axis, chromosome. Y-axis, $-\log_{10}(p)$, p values converted from *qtl2* LOD score. Rectangles mark regions with multiple genes of interest defined in *Results*.

produce a single additive p value per pathway (see Suppl. Figure 1 and **Materials and Methods** for a more detailed explanation). The key biologically significant genes and pathways significantly associated with FPG or BGD phenotypes are summarized in Fig. 3 and Table 1, while the p-values for each gene and pathway are available in Suppl. Tables 2–9).

Some of the same genes and pathways were associated with both spontaneous and radiation-induced DNA repair (*i.e.* both BGD and FPG phenotypes). Out of 63 genes that were significantly associated with FPG induced by all three radiation qualities, 44 genes were also linked with BGD, while 19 genes were specific to FPG and 343 genes specific to BGD. This high overlap is consistent with our previous results that spontaneous DNA repair can be used as a biomarker of radiation sensitivity observed in radiotherapy patients (Pariset et al., 2020a), just like FPG is a biomarker for radiation sensitivity in mice *in vivo* (Pariset et al., 2020b). In addition, the high number of genes associated with BGD compared to FPG phenotype indicates that background DNA repair is determined by a wide variety of genetic factors, while DNA repair in response to an environmental stressor is regulated by comparatively few

genes.

The shared genes that were associated with both FPG and BGD primarily fell into pathways associated with cell signal transduction and metabolism, as well as the nervous system (Fig. 3B). Meanwhile, the pathways linked with transport and chromatin organization were specific to radiation responses (FPG) and not spontaneous DNA damage (BGD), likely influenced by the fact that ionizing radiation leads to chromatin remodeling (Costes et al., 2010). On the other hand, cellular development and hemostasis as well as extracellular matrix organization (both of which are clusters of pathways involved in immune/hematopoietic responses) were linked with background (BGD) DNA repair.

3.3. Comparing early and late DNA damage responses

In addition to quantifying the genes and pathways that were significantly associated with DNA repair across all time points, we split the time points into early (4 and 8 h after irradiation) and late (24 and 48 h after irradiation), representing initial DNA repair and persistent DNA damage and repair respectively.

The genes and pathways associated with early and late responses (Fig. 4 and Suppl. Tables 4–9) partially overlapped: out of the 56 genes shared between all radiation qualities early and 94 late, 24 overlapped (Fig. 4A) with the main functions including DNA damage and tumorigenesis (*Cables1, Chst9, Dpysl3, Prkcb, Prkn*), the nervous system (*Dpysl3, Gls, Kcnn2, Mcph1, Ncald, Prkn*) and the immune/hematopoietic systems (*Flt3, Fut10, Il1rapl2, Rab7b, Stat4, Taf4b, Vps45*). Thus, these genes may be described as associated with a persistent phenotype of ionizing radiation.

Out of the 4 pathways shared between all radiation qualities early and 8 late, only 1 ("Neuronal system") overlapped (Fig. 4A, Suppl. Tables 8–9). In addition, both time points also involved either glycosaminoglycan (late) or heparan sulfate (a specific type of glycosaminoglycan; early) metabolism. Glycosaminoglycans are expressed on most mammalian cells and are involved in cell signaling during carcinogenesis, including in the nervous system, as well as inflammation (Afratis et al., 2012; Morla, 2019). Out of the non-overlapping pathways and genes, early responses primarily involved nervous system functions, while late response pathways were involved in cell signaling and cellular metabolism.

3.4. Comparing responses to high and low LET radiation

Comparing the genes and pathways associated with FPG responses across all irradiation qualities, the strongest overlap was later after irradiation (Fig. 4A): 94 genes / 8 pathways compared to 56 genes / 4 pathways, indicating that radiation quality is more likely to affect initial, but not persistent DNA damage.

At early time points after irradiation the strongest overlap was between 600 MeV/n ^{56}Fe and X-rays, possibly associated with the fact that these two qualities resulted in the highest doses: up to 0.82 Gy 600 MeV/n ^{56}Fe, up to 4 Gy X-ray, compared to 0.5 Gy 350 MeV/n ^{40}Ar. These pathways primarily involved cell signaling via MAP kinases, which have a wide range of pro-inflammatory and tumorigenic functions, as well as RHO GTPases (Fig. 4C, D). RHO GTPases regulate cellular dynamics, including cell cycle and cellular migration (Hodge and Ridley, 2016). They are involved in adverse cancer responses to therapeutic radiation, specifically, the formation of radiation-induced metastases (Burrows et al., 2013; Zhai et al., 2006), therefore are promising cellular targets for cancer treatment.

Other overlapping pathways between 600 MeV/n ^{56}Fe and X-ray irradiation included cell death signaling via NRAGE. NRAGE plays a role in homologous recombination, which is the primary repair mechanism of double-stranded DNA breaks (Yang et al., 2016), and has a complex role in carcinogenesis: it suppresses metastasis, but also increases radiation resistance, which is harmful in the context of therapeutic radiation (though advantageous in the context of space radiation). In contrast, the
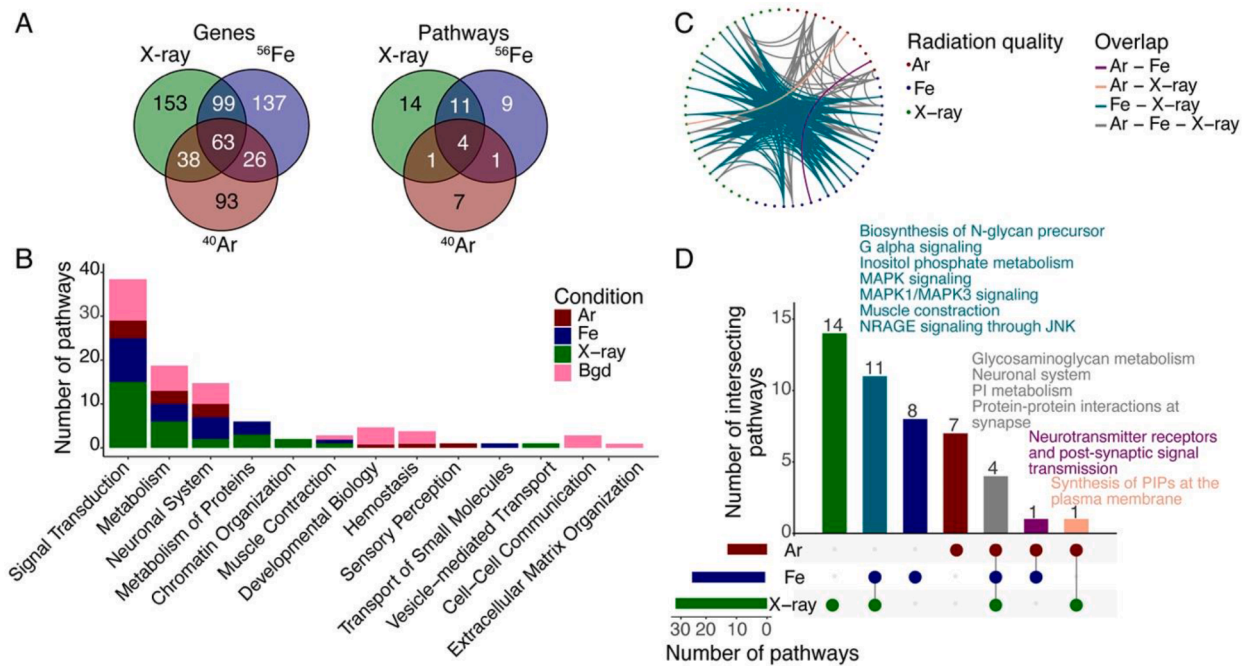
Fig. 3. SNP, gene and pathway associations with DNA damage among radiation qualities. **A, B.** Diagrams of overlapping pathways among different radiation qualities. **C.** Bar graph of significantly enriched pathways in response to different radiation qualities and time points. Major pathway groups are listed on the X axis. **D.** UpSet diagram of overlapping pathways among radiation qualities across all time points. Pathways that overlap among multiple radiation qualities are listed in text insets shaded with matching color to the bars (teal: X-ray and 600 MeV/n ^{56}Fe, orange: 350 MeV/n ^{40}Ar and X-ray, purple: 350 MeV/n ^{40}Ar and 600 MeV/n ^{56}Fe, gray: all three radiation qualities). Radiation qualities: X-rays, 350 MeV/n ^{40}Ar and 600 MeV/n ^{56}Fe.

pathways at early time points that were shared by high-LET particle, but *not* X-ray irradiation, were primarily focused on nervous system functions and glycosaminoglycan metabolism.

At later time points after irradiation we observed increased overlap in genes and pathways that were involved in high-LET particle radiation responses (600 MeV/n ^{56}Fe and 350 MeV/n ^{40}Ar), but were not shared with low-LET X-ray responses (Fig. 4A, B), likely due to the clustering and persistence of RIFs that are characteristic of high-LET particle irradiation (Penninckx et al., 2019). The high LET-specific pathways primarily regulate cell signaling via G alpha proteins and p75 receptors (Fig. 4C, E), indicating them as suitable targets for high LET radioprotection and reduction of persistent DNA damage. Both G proteins and p75 signaling are associated with tumorigenesis (Johnston et al., 2007; Maziarz et al., 2020; Suzuki et al., 2009), and p75 is also involved in neurodegeneration (Knowles et al., 2009).

Finally, we uncovered multiple gene and pathway-level associations between radiation-induced DNA damage and the nervous system. Ionizing radiation is a major neurotoxic factor: high-LET particles have been shown to cause neuroinflammation, neurodegeneration and behavioral deficits in inbred C57BL/6 J and transgenic Tg(Thy1-EGFP) MJrsJ mice (Krukowski et al., 2021; Parihar et al., 2016). However, our results suggest that different mouse strains might not be equally susceptible to ionizing radiation-induced neurotoxicity.

Most of the genes (*e.g. Dpysl, Prkn, Gls*) that were associated with *in vitro* radiosensitivity have systemic functions in regulating oxidative stress, mitochondrial functions and carcinogenesis (Kang et al., 2019; Matsunuma et al., 2018; Wang et al., 2010), in addition to their involvement in neurodegeneration (Lynch et al., 2018; Manivannan et al., 2013; Yoshino et al., 2022). The variety of functions might explain why these genes were identified in fibroblast radiation responses *in vitro* and suggests them as peripheral biomarkers of neurological risk for future experimental validation.

3.5. Comparative radiosensitivity of 15 mouse strains

The majority of mouse studies on spaceflight and simulated space radiation have been conducted using only a few inbred strains, primarily C57BL/6 and BALB/c, or transgenic mouse lines with these strains as a background. However, our results indicate major differences in radiosensitivity between mouse strains and suggest deliberately selecting them based on experimental goals instead.

A representative comparison between mouse strains is presented in Fig. 5. In this figure, all 15 strains are ranked based on the phenotype of interest, which is selected to be the average FPG at all time points and in response to all radiation qualities. In addition, the SNPs that mapped to selected carcinogenic and neurodegenerative genes (*Mcph, Ncald, Kcnn2, Gls, Dpysl3, Prkn, Cables1, Chst9, Prkcb*) that were significantly associated with FPG in the same conditions (*i.e.* shared by all time points and all radiation qualities) are listed for each mouse strain. The nucleotides are colored blue to match the one found in the most radioresistant strain (CC019) and yellow to match the most radiosensitive strain (CBA).

This representative example shows the wide variability between mouse strains both in radiation-induced DNA damage responses and in the genotypes associated with it. Specifically, multiple CC strains (CC019, CC051 CC040, CC013) are comparatively radioresistant, while CC002, CH3 and CBA are particularly radiosensitive. Thus, using a combination of these strains in an experiment would be beneficial by covering a broader range of radiation responses, in this way reducing the probability of a response that does not reach a threshold or the opposite confounding factor of a response that is too strong and saturates the measurement. Furthermore, individual mouse strains might be selected based on interest in a specific gene or a group of genes with shared functions (*e.g.* neurodegeneration) or a particular radiation quality, dose or timepoint.

Table 1
Pathways significantly associated with FPG and BGD phenotypes.

PATHWAY NAME	P VALUE	FDR-ADJUSTED P VALUE	FUNCTION
FPG, 350 MeV/n ^{40}Ar			
O-linked glycosylation	6.33E-07	0.000535	Metabolism
RAC1 GTPase cycle	3.60E-06	0.000535	Cell signaling
RHO GTPase cycle	1.73E-06	0.000978	Cell signaling
Rab regulation of trafficking	3.44E-06	0.001455	Transport
Signaling by Rho GTPases	6.82E-06	0.001923	Cell signaling
Signaling by Rho GTPases, Miro GTPases and RHOBTB3	5.88E-06	0.001923	Cell signaling
Protein-protein interactions at synapses	1.61E-05	0.003883	Nervous system
Cell junction organization	2.38E-05	0.005033	Cell structure
Phase II - Conjugation of compounds	9.06E-05	0.013942	Metabolism
RAC2 GTPase cycle	9.03E-05	0.013942	Immune system
RAB GEFs exchange GTP for GDP on RABs	8.75E-05	0.013942	Transport
CDC42 GTPase cycle	0.000248	0.034939	Transport
Neuronal System	0.000278	0.036148	Nervous system
Transport of bile salts and organic acids, metal ions and amine compounds	0.000302	0.036442	Transport
Metabolism of amino acids and derivatives	0.000393	0.044387	Metabolism
FPG, 600 MeV/n ^{56}Fe			
Protein-protein interactions at synapses	1.22E-16	2.06E-13	Nervous system
Neuronal System	9.42E-14	7.97E-11	Nervous system
Neurexins and neuroligins	9.64E-10	5.44E-07	Nervous system
Trafficking of AMPA receptors	1.40E-08	4.73E-06	Nervous system
Glutamate binding, activation of AMPA receptors and synaptic plasticity	1.40E-08	4.73E-06	Nervous system
Transmission across Chemical Synapses	4.45E-06	0.001255	Nervous system
Nuclear Envelope Breakdown	9.11E-06	0.001933	Cell division
Cell junction organization	9.14E-06	0.001933	Cell structure
RAC1 GTPase cycle	1.12E-05	0.00211	Cell signaling
CDC42 GTPase cycle	1.85E-05	0.002609	Transport
Glycolysis	1.79E-05	0.002609	Metabolism
Nervous system development	1.68E-05	0.002609	Nervous system
Synthesis of PIPs at the plasma membrane	2.03E-05	0.002638	Cell structure
Signaling by MET	3.97E-05	0.004795	Cell signaling
RHO GTPase cycle	4.26E-05	0.004805	Cell signaling
Neurotransmitter receptors and postsynaptic signal transmission	5.53E-05	0.005848	Nervous system
Cell-Cell communication	6.82E-05	0.006789	Cell signaling
Axon guidance	8.37E-05	0.007872	Nervous system Ce
Mitotic Prophase	0.00011	0.009794	Cell division
Signaling by Rho GTPases	0.00017	0.014363	Cell signaling
Signaling by Rho GTPases, Miro GTPases and RHOBTB3	0.000248	0.020014	Cell signaling
RAC3 GTPase cycle	0.000392	0.030156	Nervous system
GPCR downstream signaling	0.000522	0.038371	Cell signaling
NRAGE signals death through JNK	0.000623	0.043912	Cell death
FPG, X-ray			
Neuronal System	1.83E-15	3.09E-12	Nervous system
Protein-protein interactions at synapses	6.59E-12	5.58E-09	Nervous system
Transmission across Chemical Synapses	6.57E-10	3.71E-07	Nervous system
RHO GTPase cycle	4.71E-09	1.60E-06	Cell signaling
Activation of kainate receptors upon glutamate binding	4.74E-09	1.60E-06	Nervous system
Neurotransmitter receptors and postsynaptic signal transmission	8.15E-09	2.30E-06	Nervous system
GPCR downstream signaling	1.69E-08	4.08E-06	Cell signaling
Opioid Signalling	5.21E-08	9.89E-06	Nervous system

Table 1 (*continued*)

PATHWAY NAME	P VALUE	FDR-ADJUSTED P VALUE	FUNCTION
Neurexins and neuroligins	5.26E-08	9.89E-06	Nervous system
G alpha (q) signaling events	2.05E-07	3.46E-05	Cell signaling
Signaling by GPCR	2.87E-07	4.41E-05	Cell signaling
Signaling by Rho GTPases, Miro GTPases and RHOBTB3	1.85E-06	0.000241	Cell signaling
Heparan sulfate/heparin (HS-GAG) metabolism	1.82E-06	0.000241	Cell metabolism
Signaling by Rho GTPases	3.13E-06	0.000353	Cell signaling
Integration of energy metabolism	3.09E-06	0.000353	Cell metabolism
G alpha (s) signaling events	2.66E-05	0.002496	Cell signaling
PI5P, PP2A and IER3 Regulate PI3K/AKT Signaling	2.53E-05	0.002496	Cell signaling
RHOC GTPase cycle	2.50E-05	0.002496	Cell signaling
PLC beta mediated events	3.39E-05	0.00302	Cell signaling
RAC1 GTPase cycle	3.65E-05	0.003088	Cell signaling
Platelet homeostasis	3.90E-05	0.003139	Hematopoietic system
Negative regulation of the PI3K/AKT network	4.23E-05	0.003254	Cell signaling
Phase 0 - rapid depolarization	4.45E-05	0.003272	Cardiac functions
Cardiac conduction	7.88E-05	0.005552	Cardiac functions
G-protein mediated events	9.10E-05	0.00616	Cell signaling
G alpha (12/13) signaling events	0.000107	0.006994	Cell signaling
Regulation of insulin secretion	0.000112	0.006999	Metabolism
RHOG GTPase cycle	0.000123	0.007445	Cell signaling
G alpha (i) signaling events	0.000146	0.008547	Cell signaling
Glycosaminoglycan metabolism	0.000171	0.009656	Metabolism
RAC3 GTPase cycle	0.000214	0.011691	Nervous system
O-linked glycosylation	0.000277	0.014659	Metabolism
Metabolism of carbohydrates	0.000293	0.015046	Metabolism
Nervous system development	0.00031	0.015432	Nervous system
CDC42 GTPase cycle	0.00035	0.016908	Transport
Clathrin-mediated endocytosis	0.000381	0.017888	Nervous system
Axon guidance	0.000426	0.019461	Nervous system
RHOA GTPase cycle	0.000814	0.03624	Cell signaling
Potassium Channels	0.000859	0.037272	Nervous system
NRAGE signals death through JNK	0.000978	0.041353	Cell death
Regulation of actin dynamics for phagocytic cup formation	0.001043	0.043048	Cell signaling
Background			
Axon guidance	1.84E-10	1.55E-07	Nervous system
Nervous system development	9.88E-11	1.55E-07	Nervous system
RAC1 GTPase cycle	4.22E-09	1.74E-06	Nervous system
Neurotransmitter receptors and postsynaptic signal transmission	5.16E-09	1.74E-06	Nervous system
Cell-cell junction organization	3.22E-09	1.74E-06	Cell adhesion
MET promotes cell motility	1.75E-08	4.93E-06	Cell motility
Hemostasis	2.11E-08	5.10E-06	Hematopoietic system
Neuronal System	1.56E-07	3.31E-05	Nervous system
Cell junction organization	6.66E-07	0.000125	Cell adhesion
Developmental Biology	1.74E-06	0.00026	Cell development
Factors involved in megakaryocyte development and platelet production	2.30E-06	0.00026	Hematopoietic system
RHO GTPase cycle	2.09E-06	0.00026	Cell signaling
Transmission across Chemical Synapses	1.96E-06	0.00026	Nervous system
Protein-protein interactions at synapses	2.22E-06	0.00026	Nervous system
Cell-Cell communication	1.77E-06	0.00026	Cell signaling
Opioid Signalling	3.20E-06	0.000339	Nervous system
Platelet homeostasis	3.78E-06	0.000376	Hematopoietic system
Inwardly rectifying $K+$ channels	4.33E-06	0.000407	Nervous system
	1.01E-05	0.000898	Metabolism

Table 1 (*continued*)

PATHWAY NAME	P VALUE	FDR-ADJUSTED P VALUE	FUNCTION
Heparan sulfate/heparin (HS-GAG) metabolism			
VEGFA-VEGFR2 Pathway	1.46E-05	0.001233	Angiogenesis
Integrin cell surface interactions	1.68E-05	0.001351	Cell adhesion
Metabolism of lipids	6.67E-05	0.005124	Metabolism
Metabolism of steroids	6.97E-05	0.005124	Metabolism
Phospholipid metabolism	9.27E-05	0.006535	Metabolism
Glycosaminoglycan metabolism	0.000101	0.00686	Metabolism
Signaling by VEGF	0.000136	0.008881	Angiogenesis
RAC2 GTPase cycle	0.000205	0.012873	Cell signaling
Integration of energy metabolism	0.000302	0.018242	Metabolism
Signaling by MET	0.000481	0.028063	Cell motility
RAC3 GTPase cycle	0.000603	0.033999	Nervous system
Cardiac conduction	0.000721	0.038117	Cardiac functions
RHOG GTPase cycle	0.000701	0.038117	Cell signaling
EPH-Ephrin signaling	0.000925	0.047418	Cell development

4. Discussion

Currently the health risk from ionizing radiation exposure is typically estimated using health records of survivors of the atomic bombs in Japan and nuclear reactor workers (Cardis et al., 1995, 2007; Preston et al., 2004, 2003a, 2007; Preston et al., 2003b), who have been exposed mainly to low-LET gamma radiation. However, the translatability of health effects induced by low-LET radiation to predictions of high-LET radiation-induced risks is limited (Cucinotta, 2015), because some forms of physiological damage, for example, impairments in angiogenesis and immune responses, are unique to high-LET radiation (Paul et al., 2020; Wuu et al., 2020). As a result, model organisms are essential tools to understand space-relevant radiation responses *in vivo* (Barcellos-Hoff et al., 2015).

In particular, mice are commonly used to model genotype-phenotype associations in human diseases due to high similarities between genomes (Mouse Genome Sequencing et al., 2002). A recent study used genetically diverse HS/Npt stock mice to characterize high-LET particle-induced tumor formation *in vivo* (Edmondson et al., 2020) and compared them to spontaneous and gamma-ray-induced tumors. The tumor histotypes developed by the mice were strongly heritable, however, neither high-LET particles nor low-LET gamma radiation were shown to have a specific histotype signature. Thus, we may conclude that there is low correlation between low and high LET responses across the population, but high correlation between the responses of an individual with the same genetic background to both low and high LET radiation. Therefore, it is important to account for genetic background when attempting to predict the high LET responses from low LET responses. In addition, individual differences in radiation responses are governed by epigenetic and environmental factors, *e.g.*, sex, age (*e.g.*, age at exposure, attained age), lifestyle (smoking, alcohol, diet), comorbidity and coexposures (Locke and Weil, 2016).

There are several discrepancies between space radiation encountered
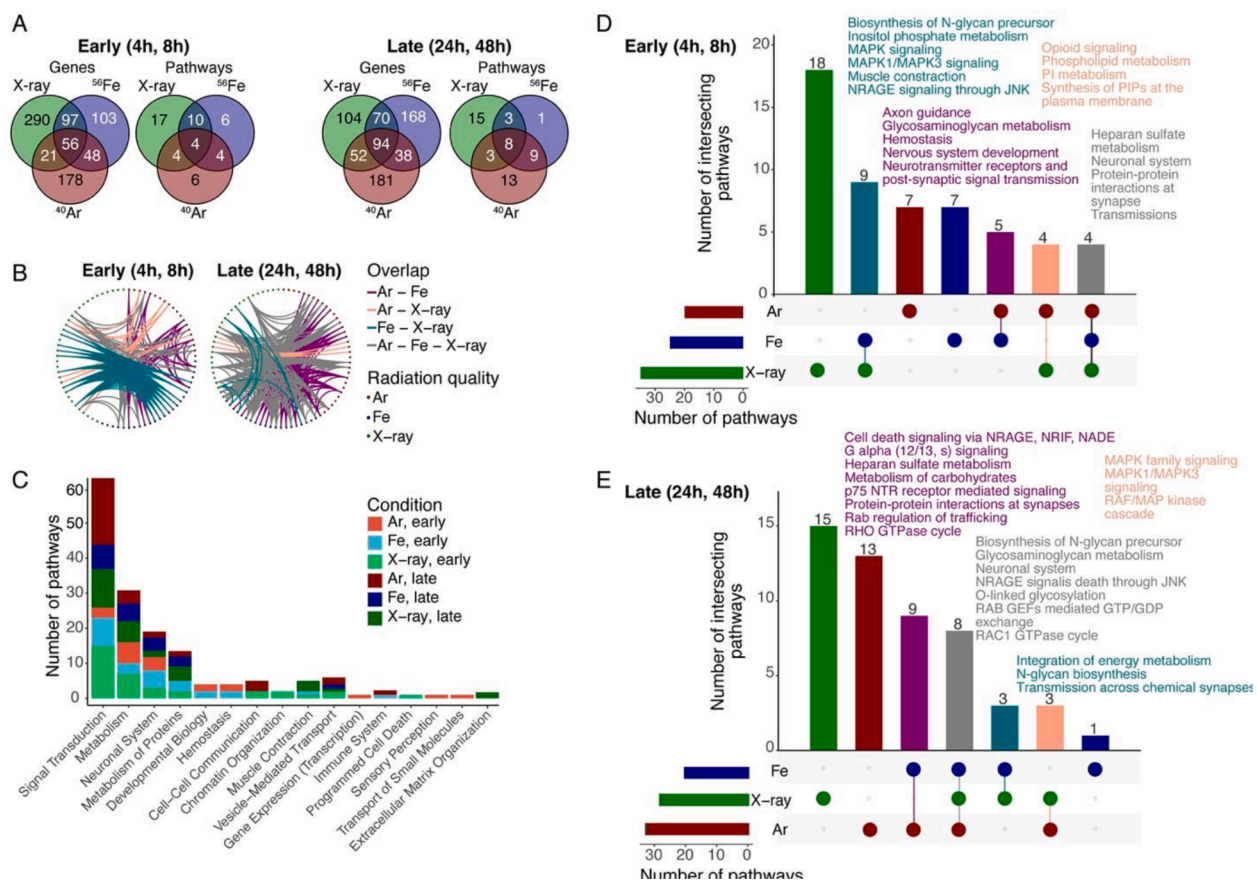
Fig. 4. SNP, gene and pathway associations with DNA damage at different time points after irradiation. A, B. Diagrams of overlapping pathways among different radiation qualities. **C.** Bar graph of significantly enriched pathways in response to different radiation qualities and time points. Major pathway groups are listed on the X axis. **D, E.** UpSet diagram of overlapping pathways among radiation qualities early (**D**, 4 – 8 h) and late (**E**, 24 – 48 h) after irradiation. Pathways that overlap among multiple radiation qualities are listed in text insets shaded with matching color to the bars (teal: X-ray and 600 MeV/n ^{56}Fe, orange: 350 MeV/n ^{40}Ar and X-ray, purple: 350 MeV/n ^{40}Ar and 600 MeV/n ^{56}Fe, gray: all three radiation qualities). Radiation qualities: X-rays, 350 MeV/n ^{40}Ar and 600 MeV/n ^{56}Fe.

			CC019	CC051	CC040	CC013	CC042	C57	CC061	B6C3	CC011	BALBC	CC037	CC032	CC002	CH3	CBA
FPG	4h	Ar	3.807	4.653	3.734	4.447	4.599	4.713	5.270	4.738	5.985	5.466	4.969	7.344	6.154	5.279	5.596
		Fe	2.403	3.242	2.782	3.266	3.015	3.189	3.488	3.673	3.632	3.394	4.485	3.934	4.265	4.374	4.510
		X-ray	1.532	1.988	2.731	2.264	2.353	2.789	2.681	2.820	2.378	2.791	2.652	2.413	4.013	3.887	3.730
	8h	Ar	1.380	1.351	1.904	1.195	1.488	1.787	1.640	1.861	1.951	2.308	1.379	3.130	1.399	1.778	2.061
		Fe	2.141	2.302	2.198	2.009	2.562	2.806	2.522	2.888	2.712	2.875	3.352	2.557	2.521	3.315	3.584
	24h	Ar	0.548	0.373	0.947	0.719	0.708	0.713	0.676	0.858	0.697	0.942	0.907	0.818	0.791	0.788	0.764
		Fe	0.826	0.991	0.849	1.008	1.152	1.165	1.123	1.242	1.119	1.137	1.545	1.118	1.429	1.508	1.554
		X-ray	0.062	0.148	0.155	0.166	0.205	0.203	0.213	0.168	0.155	0.232	0.203	0.195	0.252	0.268	0.300
	48h	Ar	0.657	0.770	0.817	1.044	0.931	1.013	1.272	0.969	1.071	1.098	1.192	0.918	1.415	1.186	1.333
		Fe	0.210	0.470	0.429	0.550	0.707	0.852	0.422	0.769	0.478	0.501	0.702	0.472	0.648	0.980	1.007
		X-ray	0.168	0.224	0.267	0.286	0.359	0.333	0.324	0.296	0.330	0.352	0.321	0.333	0.421	0.495	0.547
	AVERAGE		1.249	1.501	1.528	1.541	1.643	1.779	1.785	1.844	1.864	1.918	1.973	2.112	2.119	2.169	2.271

Gene	SNP	Chromosome	Position	CC019	CC051	CC040	CC013	CC042	C57	CC061	B6C3	CC011	BALBC	CC037	CC032	CC002	C3H	CBA
Mcph	UNCHS022348	8	18621820	A	A	A	A	A	A	G	H	A	G	G	G	G	G	G
Mcph	UNCHS022349	8	18650955	C	C	C	C	C	C	T	H	C	T	T	T	T	T	T
Mcph	UNCHS022350	8	18653081	C	C	C	C	C	C	T	H	C	T	T	C	T	T	T
Mcph	UNCHS022353	8	18707691	T	T	T	T	T	T	G	H	T	G	G	G	G	G	G
Mcph	UNCHS022355	8	18742167	A	A	A	A	A	A	G	H	A	G	G	A	G	G	G
Mcph	UNCHS022359	8	18852987	T	T	T	T	T	T	C	H	T	C	C	C	C	C	C
Mcph	UNCHS022361	8	18876471	G	G	G	G	G	G	A	H	A	A	A	A	A	A	A
Ncald	UNC25388803	15	37536110	A	A	A	A	G	G	A	G	A	G	A	G	G	G	G
Ncald	UNCHS040059	15	37546312	T	T	T	T	C	C	C	C	C	C	C	C	C	C	C
Kcnn2	UNC29171066	18	45470019	A	A	A	A	C	C	C	C	A	C	C	C	H	C	C
Kcnn2	UNCHS046160	18	45628909	A	A	A	A	G	G	G	G	A	G	G	G	G	G	G
Kcnn2	JAX00082940	18	45636871	G	G	G	G	T	T	T	T	G	T	T	T	H	T	T
Gls	UNC667964	1	52186689	G	G	G	A	A	A	G	A	A	A	A	A	A	A	A
Gls	UNC668252	1	52223330	T	T	T	C	C	C	T	C	T	C	C	C	C	C	C
Gls	UNC668320	1	52232161	C	C	C	T	T	T	C	T	C	T	T	T	T	T	T
Dpysl3	UNC29140796	18	43433921	T	T	T	T	C	C	C	C	T	C	C	C	C	C	C
Dpysl3	UNCHS046125	18	43452308	A	A	G	G	A	A	A	A	G	A	A	A	H	A	A
Dpysl3	UNCHS046126	18	43454791	A	A	A	A	G	G	G	G	A	G	G	G	G	G	G
Dpysl3	UNCHS046129	18	43464152	C	C	C	C	T	T	T	T	C	T	T	T	N	T	T
Dpysl3	UNC29141664	18	43482605	T	T	T	T	C	C	C	C	T	C	C	C	C	C	C
Prkn	UNC27565801	17	11286052	G	G	G	G	A	G	A	H	A	G	G	G	G	A	A
Prkn	JAX00073560	17	11290197	C	C	C	C	T	C	T	H	C	C	C	C	C	T	T
Prkn	UNC27566172	17	11318508	C	C	C	C	T	C	T	H	T	T	T	C	C	T	T
Prkn	UNCHS043700	17	11320714	G	G	G	G	A	G	A	H	A	G	G	G	G	A	A
Prkn	UNCHS043701	17	11339924	C	C	C	C	T	C	T	H	T	T	C	C	C	T	T
Prkn	UNC27566656	17	11360436	A	A	G	A	A	G	A	G	G	G	G	G	G	G	G
Prkn	UNC27567468	17	11422695	T	T	G	T	T	G	T	G	T	G	G	G	G	G	G
Prkn	UNC27569345	17	11565211	T	T	T	T	C	T	C	H	C	T	T	T	C	C	C
Prkn	UNC27571806	17	11732326	T	T	T	T	G	T	G	H	G	G	T	T	G	G	G
Prkn	UNC27572884	17	11818001	G	G	G	G	A	G	A	H	A	G	G	G	A	A	A
Prkn	JAX00431705	17	11834997	G	G	G	G	A	G	A	H	A	G	G	G	A	A	A
Prkn	UNCHS043713	17	11894309	C	C	C	C	T	C	T	H	T	T	C	C	T	T	T
Prkn	UNCHS043714	17	11901292	C	C	T	C	C	T	C	T	T	T	T	T	C	T	T
Prkn	UNC27574920	17	11991948	G	G	G	G	A	G	A	H	G	G	G	G	A	A	A
Prkn	UNC27576134	17	12104389	A	A	A	A	A	A	A	H	G	G	A	A	A	G	G
Prkn	UNCHS043722	17	12137802	C	C	C	C	T	C	T	H	C	T	C	C	T	T	T
Prkn	UNCHS043727	17	12190999	C	C	C	C	T	C	T	C	N	T	C	C	T	-	-
Prkn	UNCHS043728	17	12194338	C	C	C	C	T	C	T	C	N	T	C	C	T	-	-
Cables 1	UNC28737078	18	11993766	A	A	A	A	G	A	G	H	A	G	A	A	A	G	G
Cables 1	JAX00452027	18	12062217	A	A	A	A	A	G	A	G	G	G	G	G	G	G	G
Chst9	UNC28785042	18	15724201	A	A	A	A	G	G	G	G	G	G	G	G	G	G	G
Chst9	UNCHS045559	18	15726078	G	G	G	G	A	A	A	A	A	A	A	A	A	A	A
Chst9	UNC28785947	18	15795860	A	A	A	A	A	G	A	G	G	G	G	G	G	G	G
Chst9	UNCHS045561	18	15800294	A	A	A	A	A	G	A	G	G	G	G	G	G	G	G
Chst9	UNC28786205	18	15810624	T	T	T	T	C	C	C	C	C	C	C	C	C	C	C
Prkcb	UNC13751107	7	121901674	T	T	T	T	T	C	T	C	T	C	C	T	C	C	C
Prkcb	UNCHS021385	7	121965340	A	A	G	G	G	G	A	G	G	G	G	A	G	G	G
Prkcb	UNCHS021386	7	121967878	C	C	T	C	C	T	C	T	C	T	T	T	T	T	T
Prkcb	UNC13752113	7	121978472	G	G	A	G	G	A	G	A	G	A	A	A	G	A	A
Prkcb	UNCHS021393	7	122155425	T	T	T	T	T	C	T	C	T	C	C	T	T	C	C
Prkcb	UNC13754066	7	122158829	C	C	C	C	C	A	C	A	C	A	A	C	A	A	A
Prkcb	JAX00653851	7	122207014	G	G	A	A	A	A	G	A	A	A	A	A	G	A	A
Prkcb	UNC13755033	7	122223931	C	C	T	C	C	T	C	T	C	T	T	T	C	T	T
Prkcb	UNCHS021395	7	122250360	A	A	C	A	A	C	A	C	A	C	C	C	A	C	C
Prkcb	UNCHS021396	7	122254548	A	A	G	G	G	G	A	G	G	G	G	A	G	G	G

Fig. 5. A representative example of comparative radiosensitivity of 15 mouse strains. Top table, FPG in response to different radiation qualities and time points. Strains are ranked by average FPG. Bottom table, SNPs mapped to selected genes with neurological and carcinogenic functions that were significantly associated with FPG across all radiation qualities and time points. Only SNPs with different nucleotides in the most radiosensitive and the most radioresistant strains listed. Blue, nucleotides matching the most radioresistant strain (CC019). Yellow, nucleotides matching the most radiosensitive strain (CBA).

in the space environment and our experimental design. For example, the dose rate of 1 Gy/min is much higher than the dose rate for animal experiments conducted on the ISS, which is 0.2 - 0.4 mGy/day, as reported on the GeneLab portal (Berrios et al., 2021). Similarly, the time course of a few hours to 48 h post-exposure does not reflect the constant chronic exposure to space radiation. However, we have previously shown that persistent DNA damage foci observed 24 h post-exposure are a robust surrogate marker of *in vivo* lung cancer risk in mice (Ochola et al., 2019), indicating that our short-term endpoints are relevant to long-term cancer risks.

In addition, one specific distinction of high-LET HZE particles used in this study, such as ^{56}Fe 600 MeV/n, is that these particles can lead to doses as high as 1 Gy for cells being traversed, depending on the total volume, geometry and orientation of the cell with respect to the particle trajectory (Neumaier et al., 2012). One could therefore hypothesize that the dose rate of high-LET particles is not a critical factor to interpret the DNA damage response, because we are observing independent cellular events, primarily driven by the subcellular microdosimetry profile

(Vadhavkar et al., 2014). Specifically, at a fluence of 1.1 particles/100 μm^2, roughly one-third of the cells do not receive direct traversal of a single particle, whereas another one-third may receive two particles. In the case of space environment, these traversals will be even more sparse in the tissue, but when occurring will have the same microdosimetry profile. Finally, it has been shown by others how DNA damage persistent measured in one tissue correlate across all other tissues for the same strain (Rube et al., 2008). In addition, we have previously used this dataset to demonstrate that DNA repair kinetic in skin measured across the 10 CC strains correlate significantly with published *in vivo* data on white blood cell death rate measured in the same strains after 0.1 Gy whole body doses (Pariset et al., 2020b).

Some of our observed mouse strain differences *in vitro* radiosensitivity have been previously reported *in vivo* as well. For example, BALB/c has higher *in vitro* radiosensitivity than C57BL/6 in our study, and BALB/c mice are also known to be more susceptible to radiation-induced cancers *in vivo* than C57BL/6 (Storer et al., 1988). However, when assessed within the entire range of the 15 mouse strains used in this investigation, C57BL/6 and BALB/c are much more phenotypically and genotypically similar to each other than some of the CC strains (for example CC019 and CC032), suggesting CC as a better model to understand relative cancer susceptibility because they show more extreme differences in radiation responses.

In addition, our results suggest selecting different strains for investigating initial *vs.* persistent DNA damage, and for comparing sensitivity to low- and high-LET ionizing radiation. For initial DNA damage, picking one of the most radioresistant mouse strains (CC019/CC061) together with one the most radiosensitive strains (CC002/CH3/CBA) could be used to maximize the variability between strains independent of radiation quality. Similarly, CC019 and CH3/CBA strains would be a suitable combination for investigating LET-independent differences in residual DNA damage 24 – 48 h post irradiation. Finally, C57BL/6 J strain shows persistent DNA damage only in response to high-LET particles, as opposed to CC032 being particularly sensitive to low-LET X-rays, therefore, a combination of C57BL/6 J and CC032 could be used to evaluate the effects of LET on DNA damage and repair.

Although *in vivo* studies on CC mouse strains have been limited, similarly high variability between strains has been observed in a transgenic melanoma model (Ferguson et al., 2015), where the CC19 mouse strain, which was particularly radioresistant in our study, consistently showed little melanoma progression. On the other hand, *spontaneous* tumor development in non-transgenic CC mice (Wang et al., 2019) was not associated with our results of either *in vitro* radiosensitivity or spontaneous (background) *in vitro* DNA damage, indicating its limitations as a biomarker. Furthermore, a study on the cardiotoxic side effects of doxorubicin, a DNA double strand-break inducing agent used in chemotherapy, showed that some of the CC strains that developed the most doxorubicin cardiotoxicity *in vivo* were among the most radioresistant *in vitro* in our study (Zeiss et al., 2019), suggesting separate genomic associations with DNA damage and with tissue degeneration.

5. Conclusion

In conclusion, we performed a genome-wide association study of *in vitro* DNA damage responses to ionizing radiation in fibroblasts isolated from 15 collaborative cross and inbred mouse strains. We identified multiple SNPs, genes and pathways associated with spontaneous DNA damage and DNA damage responses to simulated deep space radiation (350 MeV/n ^{40}Ar and 600 MeV/n ^{56}Fe particles) and X-rays, which may underlie the differences in susceptibility to ionizing radiation among mouse strains. The genes and pathways were primarily linked to cellular signaling and metabolism as well as neurological impairments, and indicated different signaling cascades as suitable targets for limiting particle and X-ray radiation-induced DNA damage. Overall, this work shows how cell culture of different individuals can be used with the 53BP1$^+$radiation-induced foci assay to identify genes associated to

radiation sensitivity. In light of the biomarker study we previously published on human blood cells exposed to radiation *in vitro* (Pariset et al., 2020a), we suggest more GWAS studies should be conducted with similar assay to directly address this question in humans.

Our work serves as the first step in identifying the genes and pathways, which, following validation, will expand the application of genomic analysis to evaluate potential risk outcomes and therapeutic targets of ionizing radiation exposure during deep space travel. The availability of all 53BP1 expression-based DNA damage data for each *in vitro* culture, radiation condition and time point combined with the genomics data in the NASA GeneLab -omics database provides a new tool for our community to further dive into radiation-relevant genotype-phenotype associations. More generally, our results and our publicly accessible data could be used to select mouse strains based on their radiation-relevant genomic characteristics for space radiation studies and countermeasure development.

Data and code availability

All phenotypic and genomic data from this study are stored in the NASA GeneLab repository under GLDS-366, https://genelab-data.ndc.nasa.gov/genelab/accession/GLDS-366/ All code will be added to Supplementary Materials for reviewer access, and will be available on Github (https://github.com/duct317/Space-Radiation-Mouse-GWAS) upon publication. Raw image files are available upon request.

Declaration of Competing Interest

The authors declare that they have no known competing financial interests or personal relationships that could have appeared to influence the work reported in this paper.

The authors declare the following financial interests/personal relationships which may be considered as potential competing interests:

Supplementary materials

Supplementary material associated with this article can be found, in the online version, at doi:10.1016/j.lssr.2022.07.006.

References

Afratis, N., Gialeli, C., Nikitovic, D., Tsegenidis, T., Karousou, E., Theocharis, A.D., Pavao, M.S., Tzanakakis, G.N., Karamanos, N.K., 2012. Glycosaminoglycans: key players in cancer cell biology and treatment. FEBS J. 279, 1177–1197.

Alpen, E.L., Powers-Risius, P., Curtis, S.B., DeGuzman, R., 1993. Tumorigenic potential of high-Z, high-LET charged-particle radiations. Radiat. Res. 136, 382–391.

Alpen, E.L., Powers-Risius, P., Curtis, S.B., DeGuzman, R., Fry, R.J., 1994. Fluence-based relative biological effectiveness for charged particle carcinogenesis in mouse Harderian gland. Adv. Space Res. 14, 573–581.

Azizova, T.V., Bannikova, M.V., Grigoryeva, E.S., Rybkina, V.L., Hamada, N., 2020. Occupational exposure to chronic ionizing radiation increases risk of Parkinson's disease incidence in Russian Mayak workers. Int. J. Epidemiol. 49, 435–447.

Barcellos-Hoff, M.H., Blakely, E.A., Burma, S., Fornace Jr., A.J., Gerson, S., Hlatky, L., Kirsch, D.G., Luderer, U., Shay, J., Wang, Y., et al., 2015. Concepts and challenges in

cancer risk prediction for the space radiation environment. Life Sci Space Res (Amst) 6, 92–103.

Beheshti, A., Miller, J., Kidane, Y., Berrios, D., Gebre, S.G., Costes, S.V., 2018. NASA GeneLab project: bridging space radiation omics with ground studies. Radiat. Res. 189, 553–559.

Berrios, D.C., Galazka, J., Grigorev, K., Gebre, S., Costes, S.V., 2021. NASA GeneLab: interfaces for the exploration of space omics data. Nucleic. Acids. Res. 49, D1515–D1522.

Braganza, M.Z., Kitahara, C.M., Berrington de Gonzalez, A., Inskip, P.D., Johnson, K.J., Rajaraman, P., 2012. Ionizing radiation and the risk of brain and central nervous system tumors: a systematic review. Neuro. Oncol. 14, 1316–1324.

Broman, K.W., Gatti, D.M., Simecek, P., Furlotte, N.A., Prins, P., Sen, S., Yandell, B.S., Churchill, G.A., 2019. R/qtl2: software for mapping quantitative Trait Loci with high-dimensional data and multiparent populations. Genetics 211, 495–502.

Burrows, N., Telfer, B., Brabant, G., Williams, K.J., 2013. Inhibiting the phosphatidylinositide 3-kinase pathway blocks radiation-induced metastasis associated with Rho-GTPase and Hypoxia-inducible factor-1 activity. Radiother. Oncol. 108, 548–553.

Cardis, E., Gilbert, E.S., Carpenter, L., Howe, G., Kato, I., Armstrong, B.K., Beral, V., Cowper, G., Douglas, A., Fix, J., et al., 1995. Effects of low doses and low dose rates of external ionizing radiation: cancer mortality among nuclear industry workers in three countries. Radiat. Res. 142, 117–132.

Cardis, E., Vrijheid, M., Blettner, M., Gilbert, E., Hakama, M., Hill, C., Howe, G., Kaldor, J., Muirhead, C.R., Schubauer-Berigan, M., et al., 2007. The 15-country collaborative study of cancer risk among radiation workers in the nuclear industry: estimates of radiation-related cancer risks. Radiat. Res. 167, 396–416.

Churchill, G.A., Airey, D.C., Allayee, H., Angel, J.M., Attie, A.D., Beatty, J., Beavis, W.D., Belknap, J.K., Bennett, B., Berrettini, W., et al., 2004. The Collaborative cross, a community resource for the genetic analysis of complex traits. Nat. Genet. 36, 1133–1137.

Costes, S.V., Chiolo, I., Pluth, J.M., Barcellos-Hoff, M.H., Jakob, B, 2010. Spatiotemporal characterization of ionizing radiation induced DNA damage foci and their relation to chromatin organization. Mutat. Res. 704, 78–87.

Costes, S.V., Ponomarev, A., Chen, J.L., Nguyen, D., Cucinotta, F.A., Barcellos-Hoff, M. H., 2007. Image-based modeling reveals dynamic redistribution of DNA damage into nuclear sub-domains. PLoS Comput. Biol. 3, e155.

Cucinotta, F.A., 2015. A new approach to reduce uncertainties in space radiation cancer risk predictions. PLoS One 10, e0120717.

Cucinotta, F.A., Durante, M, 2006. Cancer risk from exposure to galactic cosmic rays: implications for space exploration by human beings. Lancet Oncol. 7, 431–435.

Cucinotta, F.A., To, K., Cacao, E., 2017. Predictions of space radiation fatality risk for exploration missions. Life Sci. Space Res. (Amst.) 13, 1–11.

Durante, M., Cucinotta, F.A., 2008. Heavy ion carcinogenesis and human space exploration. Nat. Rev. Cancer 8, 465–472.

Durinck, S., Moreau, Y., Kasprzyk, A., Davis, S., De Moor, B., Brazma, A., Huber, W., 2005. BioMart and bioconductor: a powerful link between biological databases and microarray data analysis. Bioinformatics 21, 3439–3440.

Durinck, S., Spellman, P.T., Birney, E., Huber, W., 2009. Mapping identifiers for the integration of genomic datasets with the R/Bioconductor package biomaRt. Nat. Protoc. 4, 1184–1191.

Edmondson, E.F., Gatti, D.M., Ray, F.A., Garcia, E.L., Fallgren, C.M., Kamstock, D.A., Weil, M.M., 2020. Genomic mapping in outbred mice reveals overlap in genetic susceptibility for HZE ion- and gamma-ray-induced tumors. Sci. Adv. 6, eaax5940.

Ferguson, B., Ram, R., Handoko, H.Y., Mukhopadhyay, P., Muller, H.K., Soyer, H.P., Morahan, G., Walker, G.J., 2015. Melanoma susceptibility as a complex trait: genetic variation controls all stages of tumor progression. Oncogene 34, 2879–2886.

Gasser, S., Orsulic, S., Brown, E.J., Raulet, D.H., 2005. The DNA damage pathway regulates innate immune system ligands of the NKG2D receptor. Nature 436, 1186–1190.

Hodge, R.G., Ridley, A.J., 2016. Regulating Rho GTPases and their regulators. Nat. Rev. Mol. Cell Biol. 17, 496–510.

Ingram, S.P., Warmenhoven, J.W., Henthorn, N.T., Smith, E.A.K., Chadwick, A.L., Burnet, N.G., Mackay, R.I., Kirkby, N.F., Kirkby, K.J., Merchant, M.J., 2019. Mechanistic modelling supports entwined rather than exclusively competitive DNA double-strand break repair pathway. Sci. Rep. 9, 6359.

Jassal, B., Matthews, L., Viteri, G., Gong, C., Lorente, P., Fabregat, A., Sidiropoulos, K., Cook, J., Gillespie, M., Haw, R., et al., 2020. The reactome pathway knowledgebase. Nucleic. Acids. Res. 48, D498–D503.

Johnston, A.L., Lun, X., Rahn, J.J., Liacini, A., Wang, L., Hamilton, M.G., Parney, I.F., Hempstead, B.L., Robbins, S.M., Forsyth, P.A., et al., 2007. The p75 neurotrophin receptor is a central regulator of glioma invasion. PLoS Biol. 5, e212.

Kang, R., Xie, Y., Zeh, H.J., Klionsky, D.J., Tang, D, 2019. Mitochondrial quality control mediated by PINK1 and PRKN: links to iron metabolism and tumor immunity. Autophagy 15, 172–173.

Kaplan, H.S., Hirsch, B.B., Brown, M.B., 1956. Indirect induction of lymphomas in irradiated mice. IV. Genetic evidence of the origin of the tumor cells from the thymic grafts. Cancer Res. 16, 434–436.

Kim, J.S., Krasieva, T.B., Kurumizaka, H., Chen, D.J., Taylor, A.M., Yokomori, K, 2005. Independent and sequential recruitment of NHEJ and HR factors to DNA damage sites in mammalian cells. J. Cell Biol. 170, 341–347.

Knowles, J.K., Rajadas, J., Nguyen, T.V., Yang, T., LeMieux, M.C., Vander Griend, L., Ishikawa, C., Massa, S.M., Wyss-Coray, T., Longo, F.M., 2009. The p75 neurotrophin receptor promotes amyloid-beta(1-42)-induced neuritic dystrophy *in vitro* and *in vivo*. J. Neurosci. 29, 10627–10637.

Korotkevich, G., Sukhov, V., Budin, N., Shpak, B., Artyomov, M.N., Sergushichev, A., 2021. Fast gene set enrichment analysis. bioRxiv 1, 060012.

Krukowski, K., Grue, K., Becker, M., Elizarraras, E., Frias, E.S., Halvorsen, A., Koenig-Zanoff, M., Frattini, V., Nimmagadda, H., Feng, X., et al., 2021. The impact of deep space radiation on cognitive performance: from biological sex to biomarkers to countermeasures. Sci. Adv. 7, eabg6702.

Locke, P.A., Weil, M.M., 2016. Personalized cancer risk assessments for space radiation exposures. Front. Oncol. 6, 38.

Lynch, D.S., Chelban, V., Vandrovcova, J., Pittman, A., Wood, N.W., Houlden, H., 2018. GLS loss of function causes autosomal recessive spastic ataxia and optic atrophy. Ann. Clin. Transl. Neurol. 5, 216–221.

Manivannan, J., Tay, S.S., Ling, E.A., Dheen, S.T., 2013. Dihydropyrimidinase-like 3 regulates the inflammatory response of activated microglia. Neuroscience 253, 40–54.

Matsunuma, R., Chan, D.W., Kim, B.J., Singh, P., Han, A., Saltzman, A.B., Cheng, C., Lei, J.T., Wang, J., Roberto da Silva, L., et al., 2018. DPYSL3 modulates mitosis, migration, and epithelial-to-mesenchymal transition in claudin-low breast cancer. Proc. Natl. Acad. Sci. U. S. A. 115, E11978–E11987.

Maziarz, M., Federico, A., Zhao, J., Dujmusic, L., Zhao, Z., Monti, S., Varelas, X., Garcia-Marcos, M., 2020. Naturally occurring hotspot cancer mutations in Galpha13 promote oncogenic signaling. J. Biol. Chem. 295, 16897–16904.

Morgan, A.P., Fu, C.P., Kao, C.Y., Welsh, C.E., Didion, J.P., Yadgary, L., Hyacinth, L., Ferris, M.T., Bell, T.A., Miller, D.R., et al., 2015. The mouse universal genotyping array: from substrains to subspecies. G3 (Bethesda) 6, 263–279.

Morla, S., 2019. Glycosaminoglycans and glycosaminoglycan mimetics in cancer and inflammation. Int. J. Mol. Sci. 20.

Mouse Genome Sequencing, C., Waterston, R.H., Lindblad-Toh, K., Birney, E., Rogers, J., Abril, J.F., Agarwal, P., Agarwala, R., Ainscough, R., Alexandersson, M., et al., 2002. Initial sequencing and comparative analysis of the mouse genome. Nature 420, 520–562.

National Research, C., 2006. Health Risks from Exposure to Low Levels of Ionizing Radiation: BEIR VII Phase 2. The National Academies Press, Washington, DC.

Neumaier, T., Swenson, J., Pham, C., Polyzos, A., Lo, A.T., Yang, P., Dyball, J., Asaithamby, A., Chen, D.J., Bissell, M.J., et al., 2012. Evidence for formation of DNA repair centers and dose-response nonlinearity in human cells. Proc. Natl. Acad. Sci. U. S. A. 109, 443–448.

Nguyen, T., Tagett, R., Donato, M., Mitrea, C., Draghici, S., 2016. A novel bi-level meta-analysis approach: applied to biological pathway analysis. Bioinformatics 32, 409–416.

Nyholt, D.R., 2000. All LODs are not created equal. Am. J. Hum. Genet. 67, 282–288.

Ochola, D.O., Sharif, R., Bedford, J.S., Keefe, T.J., Kato, T.A., Fallgren, C.M., Demant, P., Costes, S.V., Weil, M.M., 2019. Persistence of gamma-H2AX foci in bronchial cells correlates with susceptibility to radiation associated lung cancer in mice. Radiat. Res. 191, 67–75.

Parihar, V.K., Allen, B.D., Caressi, C., Kwok, S., Chu, E., Tran, K.K., Chmielewski, N.N., Giedzinski, E., Acharya, M.M., Britten, R.A., et al., 2016. Cosmic radiation exposure and persistent cognitive dysfunction. Sci. Rep. 6.

Pariset, E., Bertucci, A., Petay, M., Malkani, S., Lopez Macha, A., Paulino Lima, I.G., Gomez Gonzalez, V., Tin, A.S., Tang, J., Plante, I., et al., 2020a. DNA damage baseline predicts space radiation and radio-therapeutic resilience. Cell Rep. 33 https://doi.org/10.1016/j.celrep.2020.108434.

Pariset, E., Penninckx, S., Kerbaul, C.D., Guiet, E., Macha, A.L., Cekanaviciute, E., Snijders, A.M., Mao, J.H., Paris, F., Costes, S.V., 2020b. 53BP1 Repair Kinetics for Prediction of In Vivo Radiation Susceptibility in 15 Mouse Strains. Radiat. Res. 194, 485–499.

Pasqual, E., Boussin, F., Bazyka, D., Nordenskjold, A., Yamada, M., Ozasa, K., Pazzaglia, S., Roy, L., Thierry-Chef, I., de Vathaire, F., et al., 2021. Cognitive effects of low dose of ionizing radiation - Lessons learned and research gaps from epidemiological and biological studies. Environ. Int. 147, 106295.

Paul, A.M., Cheng-Campbell, M., Blaber, E.A., Anand, S., Bhattacharya, S., Zwart, S.R., Crucian, B.E., Smith, S.M., Meller, R., Grabham, P., et al., 2020. Beyond low-earth orbit: characterizing immune and microRNA differentials following simulated deep spaceflight conditions in mice. iScience 23, 101747.

Penninckx, S., Cekanaviciute, E., Degorre, C., Guiet, E., Viger, L., Lucas, S., Costes, S.V., 2019. Dose, LET and strain dependence of radiation-induced 53BP1 foci in 15 mouse strains ex vivo introducing novel DNA damage metrics. Radiat. Res. 192, 1–12.

Penninckx, S., Pariset, E., Acuna, A.U., Lucas, S., Costes, S.V., 2020. Considering cell proliferation to optimize detection of radiation-induced 53BP1-positive foci in 15 mouse strains ex vivo. Radiat. Res.

Penninckx, S., Pariset, E., Cekanaviciute, E., Costes, S.V., 2021. Quantification of radiation-induced DNA double strand break repair foci to evaluate and predict biological responses to ionizing radiation. NAR Cancer 3, zcab046.

Preston, D.L., Pierce, D.A., Shimizu, Y., Cullings, H.M., Fujita, S., Funamoto, S., Kodama, K., 2004. Effect of recent changes in atomic bomb survivor dosimetry on cancer mortality risk estimates. Radiat. Res. 162, 377–389.

Preston, D.L., Pierce, D.A., Shimizu, Y., Ron, E., Mabuchi, K., 2003a. Dose response and temporal patterns of radiation-associated solid cancer risks. Health Phys. 85, 43–46.

Preston, D.L., Ron, E., Tokuoka, S., Funamoto, S., Nishi, N., Soda, M., Mabuchi, K., Kodama, K., 2007. Solid cancer incidence in atomic bomb survivors: 1958-1998. Radiat. Res. 168, 1–64.

Preston, D.L., Shimizu, Y., Pierce, D.A., Suyama, A., Mabuchi, K., 2003b. Studies of mortality of atomic bomb survivors. Report 13: solid cancer and noncancer disease mortality: 1950-1997. Radiat. Res. 160, 381–407.

Rube, C.E., Grudzenski, S., Kuhne, M., Dong, X., Rief, N., Lobrich, M., Rube, C, 2008. DNA double-strand break repair of blood lymphocytes and normal tissues analysed in a preclinical mouse model: implications for radiosensitivity testing. Clin. Cancer Res. 14, 6546–6555.

Shibata, A., Jeggo, P.A., 2020. Roles for 53BP1 in the repair of radiation-induced DNA double strand breaks. DNA Repair (Amst.) 93, 102915.

Snijders, A.M., Langley, S.A., Kim, Y.M., Brislawn, C.J., Noecker, C., Zink, E.M., Fansler, S.J., Casey, C.P., Miller, D.R., Huang, Y., et al., 2016. Influence of early life exposure, host genetics and diet on the mouse gut microbiome and metabolome. Nat. Microbiol. 2, 16221.

Srivastava, A., Morgan, A.P., Najarian, M.L., Sarsani, V.K., Sigmon, J.S., Shorter, J.R., Kashfeen, A., McMullan, R.C., Williams, L.H., Giusti-Rodriguez, P., et al., 2017. Genomes of the Mouse Collaborative Cross. Genetics 206, 537–556.

Storer, J.B., Mitchell, T.J., Fry, R.J., 1988. Extrapolation of the relative risk of radiogenic neoplasms across mouse strains and to man. Radiat. Res. 114, 331–353.

Suzuki, N., Hajicek, N., Kozasa, T., 2009. Regulation and physiological functions of G12/13-mediated signaling pathways. Neurosignals 17, 55–70.

Tapio, S., Little, M.P., Kaiser, J.C., Impens, N., Hamada, N., Georgakilas, A.G., Simar, D., Salomaa, S., 2021. Ionizing radiation-induced circulatory and metabolic diseases. Environ. Int. 146, 106235.

Vadhavkar, N., Pham, C., Georgescu, W., Deschamps, T., Heuskin, A.C., Tang, J., Costes, S.V., 2014a. Combinatorial DNA damage pairing model based on X-ray-induced foci predicts the dose and LET dependence of cell death in human breast cells. Radiat. Res. 182, 273–281.

Wang, J.B., Erickson, J.W., Fuji, R., Ramachandran, S., Gao, P., Dinavahi, R., Wilson, K. F., Ambrosio, A.L., Dias, S.M., Dang, C.V., et al., 2010. Targeting mitochondrial glutaminase activity inhibits oncogenic transformation. Cancer Cell 18, 207–219.

Wang, P., Wang, Y., Langley, S.A., Zhou, Y.X., Jen, K.Y., Sun, Q., Brislawn, C., Rojas, C. M., Wahl, K.L., Wang, T., et al., 2019. Diverse tumour susceptibility in Collaborative Cross mice: identification of a new mouse model for human gastric tumourigenesis. Gut 68, 1942–1952.

Wang, Y., Boerma, M., Zhou, D, 2016. Ionizing radiation-induced endothelial cell senescence and cardiovascular diseases. Radiat. Res. 186, 153–161.

Wuu, Y.R., Hu, B., Okunola, H., Paul, A.M., Blaber, E.A., Cheng-Campbell, M., Beheshti, A., Grabham, P., 2020. LET-dependent low dose and synergistic inhibition of human angiogenesis by charged particles: validation of miRNAs that drive inhibition. iScience 23, 101771.

Yang, Q., Pan, Q., Li, C., Xu, Y., Wen, C., Sun, F., 2016. NRAGE is involved in homologous recombination repair to resist the DNA-damaging chemotherapy and composes a ternary complex with RNF8-BARD1 to promote cell survival in squamous esophageal tumorigenesis. Cell Death Differ. 23, 1406–1416.

Yoshino, H., Li, Y., Nishioka, K., Daida, K., Hayashida, A., Ishiguro, Y., Yamada, D., Izawa, N., Nishi, K., Nishikawa, N., et al., 2022. Genotype-phenotype correlation of Parkinson's disease with PRKN variants. Neurobiol. Aging.

Zeiss, C.J., Gatti, D.M., Toro-Salazar, O., Davis, C., Lutz, C.M., Spinale, F., Stearns, T., Furtado, M.B., Churchill, G.A., 2019. Doxorubicin-induced cardiotoxicity in collaborative cross (CC) mice recapitulates individual cardiotoxicity in humans. G3 (Bethesda) 9, 2637–2646.

Zhai, G.G., Malhotra, R., Delaney, M., Latham, D., Nestler, U., Zhang, M., Mukherjee, N., Song, Q., Robe, P., Chakravarti, A., 2006. Radiation enhances the invasive potential of primary glioblastoma cells via activation of the Rho signaling pathway. J. Neurooncol. 76, 227–237.